Image Registration Algorithm for Molecular Tagging Velocimetry Applied to Unsteady Flow in Hele-Shaw Cell

2013

F. Brunet[1,2,3,*], E. Cid[1,2], A. Bartoli[3],
E. Bouche[1,2], F. Risso[1,2], V. Roig[1,2]

[1] IMFT (Institut de Mécanique des Fluides de Toulouse), UMR 5502 CNRS and Université de Toulouse (INPT, UPS), Allée Camille Soula, Toulouse F-31400, France

[2] Fédération de recherche Fermat FR3089, Toulouse, France

[3] ISIT (Image Science for Interventional Techniques), UMR 6284 CNRS and Clermont Université (UdA), BP 10448, F-63000 Clermont-Ferrand, France

[*] Corresponding author: `florent@brnt.eu`

This work has been funded by the research federation Fermat (Fédération de recherche Fermat FR 3089, `www.federation-fermat.fr`*).*

This is a preprint version of the article. Some minor changes may exist between this version and the final one.

Please, cite this work as:
F. Brunet, E. Cid, A. Bartoli, E. Bouche, F. Risso, V. Roig, Image registration algorithm for molecular tagging velocimetry applied to unsteady flow in Hele-Shaw cell, Experimental Thermal and Fluid Science 44 (2013) – 897-904.

Absract. In order to develop velocimetry methods for confined geometries, we propose to combine image registration and volumetric reconstruction from a monocular video of the draining of a Hele-Shaw cell filled with water. The cell's thickness is small compared to the other two dimensions (*e.g.* $1 \times 400 \times 800$ mm^3). We use a technique known as molecular tagging which consists in marking by *photobleaching* a pattern in the fluid and then tracking its deformations. The evolution of the pattern is filmed with a camera whose principal axis coincides with the cell's gap. The velocity of the fluid along this direction is not constant. Consequently, tracking the pattern cannot be achieved with classical methods because what is observed is the integral of the marked molecules over the entire cell's gap. The proposed approach is built on top of direct image registration that we extend to specifically model the volumetric image formation. It allows us to accurately measure the motion and the velocity profiles for the entire volume (including the cell's gap) which is something usually hard to achieve. The results we obtained are consistent with the theoretical hydrodynamic behaviour for this flow which is known as the *Poiseuille flow*.

Keywords photobleaching, MTV (Molecular Tracking Velocimetry), Hele-Shaw, Poiseuille flow, tracking, direct image registration

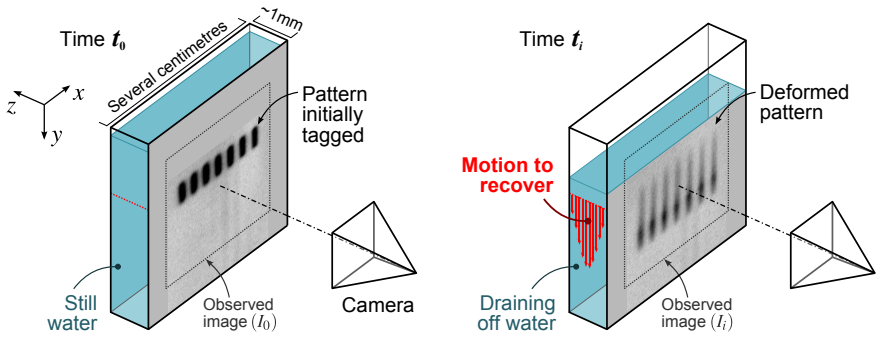

Figure 1: In this paper, we propose a new algorithm based on image registration that allows to compute the 3D motion of an unsteady fluid flow in a Hele-Shaw cell filmed with a single camera.

1 Introduction

1.1 General Context

Flows in small devices are widely used in chemical or biological applications. The design of the forces necessary to manipulate microfluidic flows as well as the control of mixing in such devices require an improvement of flow visualization and velocimetry techniques [1]. This paper applies computer vision techniques to experiments in fluid mechanics. We propose a new method based on imagery to densely and accurately measure planar flows as observed in confined geometries whatever is their depthwise velocity gradient. We chose to test the method analysing the Poiseuille flow that develops during the drainage of a Hele-Shaw cell. Figure 1 gives an overview of the experimental setup. We propose a new algorithm combining direct image registration and monocular volumetric reconstruction to track a pattern tagged into the liquid at the molecular level. Our approach allows us to make measurements with high spatial and temporal resolutions (up to 250 volumes per second with $200 \times 200 \times 40$ voxels). Previous experimental measurements of this type of flow have principally been obtained for small regions of interest (around 1 mm^3 using *e.g.* Micro Particle Image Velocimetry (μPIV) [2]) or without describing the flow inhomogeneity through the gap (using *e.g.* classical PIV [3]). Besides, our approach allows us to measure the unsteady development of the Poiseuille flow. This study is therefore a proof of concept and the first step for the development of a more general methodology providing 3D description of instantaneous planar velocity fields.

1.2 Contribution

Obtaining accurate flow measurements in a Hele-Shaw cell raises several major computer vision issues. Our goal is to obtain the flow using general and weak hypotheses so as to be able to validate the theoretical flow model *a posteriori*. We thus meet the problem of modelling the 3D motion of a liquid in a Hele-Shaw cell and of making a volumetric reconstruction of an homogeneous moving liquid from a single point of view. We propose a set of simple but physically realistic hypotheses. In particular, we consider that the flow is *lamellar* which means that the liquid acts as if it were made of an infinite number of rigid layers of infinitesimal thickness. These layers are parallel to the widest surface and move independently from each other. We approximate this model with a finite number of layers. We also make assumptions on the layers' motion: (i) the motion of the liquid is symmetric with respect to the centre of the cell, (ii) the layers are not allowed to go upward (*i.e.* the flow must be positive in the y-direction as defined on figure 1), (iii) the motion of the layers can be described as translations parallel to the y-direction, and (iv) the motion is faster at the centre of the cell than closer to the cell boundaries. We finally consider a volumetric image formation model based on the fact that pixel intensities result from an integral measurement of the concentration of tracer in the corresponding volume of the Hele-Shaw cell. With all these elements, we propose a variant of direct image registration [4] adapted to the case of the superposed layers. The beauty of our approach is that

even thought it solves a complex fluid flow estimation problem, it only requires to solve a single constrained least-squares optimization problem to obtain the 3D motion of the fluid over the whole input video.

Note also that as a side contribution, we propose an image interpolation algorithm based on regularized splines after having shown that standard bilinear and bicubic interpolation introduce a systematic bias. This is important to meet the requirement of accurate measurements.

1.3 Related Work

The 3D reconstruction of a transparent volume has been extensively reviewed in [5]. Although many computer vision methods are dedicated to opaque objects, several methods were also proposed for transparent phenomena.

Tomography [6] is a related problem. Similarly to our case, the intensity of a pixel corresponds to an integral measured over a volume along some line of sight. Our approach differs from tomography in that we only use a single camera (mainly for practical reasons including the problems of light reflection with the glass surface of the Hele-Shaw cell and the fact that high speed cameras are expensive). Tomography from a single view point has been investigated for reconstructing astronomical objects such as planetary objects [7]. As in our case, [7] partly relies on the symmetry of the objects to reconstruct but, unlike us, only reconstructs static scenes.

These previous approaches are formulated as inverse problems (with all the drawbacks of ill-conditioned problems due to noise or missing data). It is possible to make direct measurements with a proper experimental setup. For instance, [8] reconstructs clouds of smoke using a laser sheet which is swept across the volume. The laser sheet is filmed from an orthogonal point of view and the observed pixels are linked to the concentration of smoke. This kind of approach is not possible in our case because what we aim at observing is the inner motion of a completely homogeneous liquid without adding tracer particles to it. Beside, the temporal resolution of such a system would not be sufficient for our needs.

Similarly to our contribution, [9] proposes a variant of classical optical flow estimation from images. This algorithm incorporates a volumetric model of a liquid in a microchannel. However, in [9], the Poiseuille flow model is used as a strong assumption.

Paper organization We describe the experimental setup and molecular tagging based on photobleaching in §2. Our contribution is explained in §3. The results are presented in §4. We conclude and discuss the possible implications of our work in fluid mechanics in §5.

2 Experimental Setup

2.1 The Hele-Shaw Cell

The Hele-Shaw cell we used for this paper is an almost bi-dimensional cell made of two parallel plates of glass (400×800 mm^2) separated by a 1 mm wide gap. The cell we used is the same as the one used in [10]. A picture of this cell is given in figure 2. The cell is filled with water and a downward translation is generated by draining off the cell with a valve located at the bottom, in the middle of the cell. The liquid's motion is observed from a fronto-parallel point of view, *i.e.* the principal axis of the camera is orthogonal to the surface of the cell. The acquisition is done with a fast camera (Photron RS3000) at a resolution of 1024×1024 pixels with an effective intensity depth of 10 bits per pixel. The camera was equipped with a 58mm objective lens with a diaphragm aperture of 1.2. The frequency of the acquisitions is limited by the sensitivity of the camera sensor compared to the luminous intensity of the observed phenomenon. Our light source (see next paragraph) allowed us to capture 250 frames per seconds. This was sufficient for the phenomenon we wanted to observe since the velocity of the fastest part of the draining liquid is expected to be less than one pixel per frame.

2.2 Molecular Tagging Based on Photobleaching

In order to observe the fluid motion, we tagged the liquid at the molecular level with a technique known as *photobleaching* [11, 12]. It has the advantage of being truly non-invasive contrarily to other techniques such as PIV where particles are added. Such particles may have a proper motion independent of the fluid and, moreover, they may adhere to the wall of the cell. The photobleaching method is an irreversible photochemical reaction which means that phenomena lasting a relatively long time may be observed with this tagging technique. This is particularly desirable to make measurement of an unsteady flow such as in the case of the planar Poiseuille flow under study in this paper (which is a phenomenon that lasts several seconds). This property of photobleaching makes the technique eventually usable for other types of flow.

We now give the general principles of the tagging we used. A tracer, the *fluorescein*, is uniformly mixed to the water (at a concentration of 10^{-4} g.L^{-1}). In a first step, the fluorescein is marked with a continuous Argon laser beam (Spectra physics) of wavelength $\lambda_1 = 488$ nm having a luminous power of 1 W. When this lighting is maintained long enough, the properties of the fluorescein molecules are irreversibly inhibited by photobleaching [11]. In a second step, a second laser beam (New wave Pegasus) of wavelength $\lambda_2 = 527$ nm excites the unmarked fluorescein with a power of 15 W. When excited with such a light source the tracer emits light by fluorescence. This signal is acquired with a high-speed camera (Photron RS3000) equipped with a high-pass filter ($\lambda > 540$ nm). A spherical lens ($f = -12.5$ mm) is placed between the laser beam λ_2 and the cell in order to illuminate a whole area of the cell. The camera observes a fluorescent signal (bright) coming from the unmarked liquid and a lack of signal (dark) for the area where the fluorescein has been previously bleached with the laser beam λ_1 (figure 2). Note that the fluorescent signal comes uniformly from the entire volume of liquid that is excited with λ_2 (the re-absorption of the fluorescein at a concentration of 10^{-4} g.L^{-1} and at a wavelength of 527 nm is negligible on a 1 mm thick volume, see [13]). We have taken a special care concerning the potential non-uniform thermal effects that could be generated by the laser λ_2. First, we have experimentally checked that these effects are negligible by observing the effect of the illumination with λ_2 on a completely still liquid. Second, as a supplementary caution measure, we added a cooling system to the experimental setup (a fan directed at the cell). In order to create a pattern by photobleaching, the laser beam λ_1 is shaped using a cylindrical lens ($f = -40$ mm). Two mirrors oriented at 45° with respect to the cell reflect the beam which then passes through an opaque mask before marking a 'column' pattern in the liquid. Photobleaching of a column requires 15 seconds of illumination. The last mirror is translated using an automated mechanism to generate a matrix-shaped pattern. This step requires the liquid to be at rest during the marking process.

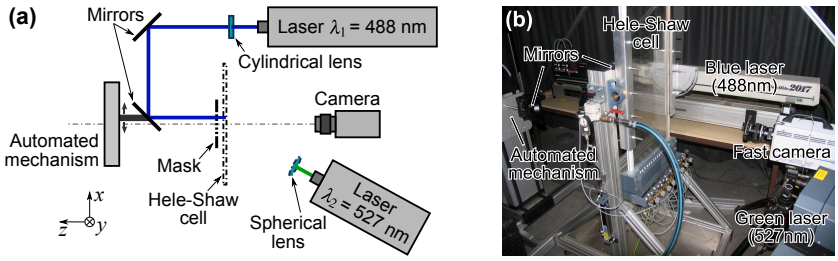

Figure 2: (a) Schematic of our setup (top view). (b) Front view of our setup.

2.3 Image Formation Model

The observed pixel intensity is linked to the concentration of non-bleached fluorescein. The important thing here is that the intensity of a pixel corresponds exactly to the relative concentrations of bleached and

[0]In the experiments of this paper, we maintained the illumination during 15 seconds for each column of marks. This duration depends mainly on the luminous power received by the liquid. In our case, it has been determined experimentally by finding the minimal marking duration giving the highest contrast.

non-bleached fluorescein integrated on the small volume of the cell that corresponds to this pixel. This is illustrated in figure 3. Note that the concentration of fluorescein is completely uniform in the entire cell ; only the relative concentration of *bleached* and *non-bleached* fluorescein may vary. In the following, we neglect perspective effects and approximate the camera model by an orthogonal projection [14]. This makes sense because the gap is small compared to the distance from the camera to the cell and because the bleached pattern is located at the centre of the acquired images.

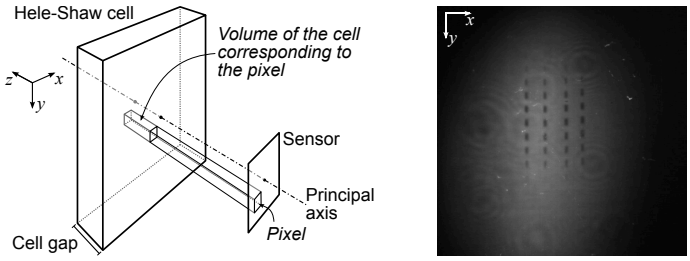

(a) (b)

Figure 3: (a) The intensity value of a pixel is proportional to the quantity of non-inhibited fluorescein in the volume of the cell corresponding to that pixel. (b) Example of acquired image: the tagged pattern is the set of aligned dark marks at the centre of the image.

3 Simultaneous Registration and Volumetric Reconstruction

In this section, we detail the algorithm that reconstruct the observed volume. We also explain the basics of classical direct image registration and why it cannot be used directly for volumetric fluid flow reconstruction.

3.1 Direct Image Registration

Image registration is the problem of finding the geometric transformation between two images. In direct image registration [4], this transformation is determined directly from the intensities of the pixels. Let R be a reference image (in our case, an image of the bleached pattern before any motion) and let I_i be the ith image of the input video (for $i = 1, \ldots, m$). If we naively consider that the motion is a simple global downward translation of magnitude t, then aligning an input image I_i to the reference R with direct image registration is formulated as:

$$\min_{t} \sum_{(x,y)\in\Omega} \left(I_i(x,y) - R\left(x, y-t\right)\right)^2, \tag{1}$$

where Ω is the *region of interest*, a portion of the input image I_i that contains the whole bleached pattern. Equation (1) is a non linear least-squares optimization problem easily solved using, for instance, a Gauss-Newton-like algorithm [15].

Formulation (1) is valid only if the Brightness Constancy Assumption is satisfied. In other words, the colours of corresponding pixels must be identical. In our case, the intensity of a pixel is the integral of the corresponding cell's volume. Since the motion of the fluid along the z-direction is not uniform, there is no direct colour correspondence between a pixel of the reference image and the corresponding pixels in the input video. Consequently, the motion of the marked pattern cannot be explained with a simple translation (see figure 4).

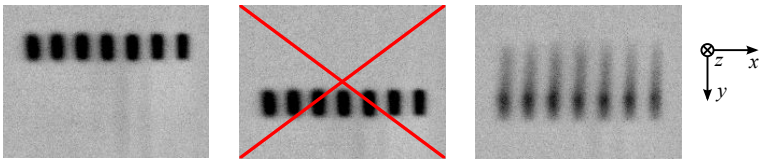

Figure 4: In our experiment, a simple tracking of the bleached pattern is not possible because the brightness constancy assumption is not satisfied. This stems from the fact that the variation of the liquid's motion across the thickness of the cell is not negligible.

3.2 The Proposed Approach

3.2.1 Motion Model and Image Formation Model

The idea of our approach lies in the model we use for the motion and for the formation of the images. As explained before, the flow we consider is lamellar. We thus consider that the volume is divided into n layers parallel to the surface of the cell. The concentration of unbleached fluorescein contained in each one of these layers is given by dividing the reference image by the number of layers (we consider that before any motion happens the concentration of bleached and unbleached fluorescein is uniform along the z-direction). Let us note L_j the intensity of the jth layer ($j = 1, \ldots, n$). We have that:

$$L_j(x,y) = \frac{1}{n} R(x,y) \qquad \text{and} \qquad R(x,y) = \sum_{j=1}^{n} L_j(x,y) \tag{2}$$

Still considering the lamellar hypothesis for the flow, the above defined layers will slide independently from each other with downward translations (see figure 5). A translation parameter $t_{i,j}$ is associated to the jth layer for the ith image of the input video ($i = 1, \ldots, m$). From this model of the volume, the image formation model is given by integrating the concentrations carried by all the translated layers and we have:

$$I_i(x,y) \approx \sum_{j=1}^{n} L_j\left(x, y - t_{i,j}\right). \tag{3}$$

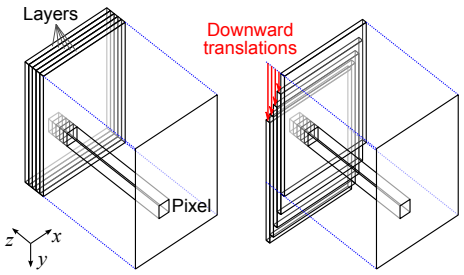

Figure 5: In our model, the intensity of a pixel is obtained by integrating the fluorescein concentration carried by the layers. A downward translation (red arrows) is associated to each one of the layers for each one of the images of the input video. These translations are the unknowns of our problem. They are determined using our algorithm extending direct image registration.

3.2.2 Additional Hypotheses

It is possible to make a few additional assumptions on the translations. These assumptions are quite simple and mainly based on the geometry of the experimental setup and on the fact that the only applied force is

gravitational:

1. *Symmetry.* The flow is symmetric with respect to the centre of the cell in the z-direction. This constraint is naturally enforced by modelling only half the cell (by convention, $t_{i,n}$ is the innermost layer while $t_{i,1}$ is the one closest to the wall).

2. *Temporal consistency.* A layer never goes upward (in other words, the translations are all 'top to bottom'), *i.e.* $t_{i+1,j} \geq t_{i,j}, \forall i \in \{1,\ldots,m-1\}, \forall j \in \{1,\ldots,n\}$.

3. *Spatial consistency.* The closer a layer to the cell's boundary, the slower, *i.e.* $t_{i,j+1} \geq t_{i,j}, \forall i \in \{1,\ldots,m\}, \forall j \in \{1,\ldots,n-1\}$.

4. *Positivity.* All the translations are downward translations. This can be enforced by simply saying that $t_{1,1} \geq 0$ (all the other translation parameters will necessarily be positive given the temporal and the spatial consistency constraints).

3.2.3 Final Optimization Problem

Our approach is formulated as an optimization problem derived from the basic formulation (1) of direct image registration. The first difference is that the image formation model based on the integration of the volumetric layers replaces the reference image in the initial formulation. The second difference is that inequality constraints are enforced on the unknowns. The third difference is that we align the whole sequence at once in order to take into account the temporal consistency hypothesis. The final optimization problem is:

$$\begin{aligned} &\min_{\mathsf{T}} \sum_{i=1}^{m} \sum_{(x,y)\in\Omega} \left(I_i(x,y) - \sum_{j=1}^{n} L_j\left(x, y - t_{i,j}\right) \right)^2 \\ &\text{subject to} \quad \begin{cases} t_{1,1} \geq 0 \\ t_{i+1,j} \geq t_{i,j} & \forall i \in \{1,\ldots,m-1\}, \forall j \in \{1,\ldots,n\} \\ t_{i,j+1} \geq t_{i,j} & \forall i \in \{1,\ldots,m\}, \forall j \in \{1,\ldots,n-1\} \end{cases} \end{aligned} \tag{4}$$

where T is an $m \times n$ matrix containing all the translation parameters to determine. Problem (4) may be solved using for instance sequential quadratic programming [16]. In practice, we used Matlab's fmincon function.

3.3 Image Interpolation

In equation (4) the input images have to be evaluated at non integer locations. Besides, we know that the order of magnitude of the translation of the central layer between two successive images is about one pixel. Consequently, sub-pixel evaluation of the images must be performed with extreme care. Common algorithms such as bilinear or bicubic interpolation may introduce a bias. This is particularly true when the non-integer locations for the interpolation all have the same fractional part (which is the case for a simple vertical translation as used in our model). A simple experiment reported in figure 6 illustrates this phenomenon. For that, we took two images I_a and I_b at the beginning of a video that we acquired before any fluid's motion. Then, we looked at the intensity difference between the first image I_a and the second image I_b translated along the y-axis by Δy pixels. This difference, denoted d, is formulated as:

$$d(\Delta y) = \sum_{(x,y)\in\Omega} \| I_a(x,y) - I_b(x, y+\Delta y) \| \tag{5}$$

Note that in the expression of d, the way the images are evaluated is very similar to the one used in the optimization problem we proposed in equation (4). Since I_a and I_b are identical (except for the noise), the difference d should be minimal for $\Delta y = 0$ pixel. Figure 6 tells us that with bilinear or bicubic interpolation, $\Delta y = 0$ correspond to a local maximum and that two local minima appear on each side of $\Delta y = 0$ for

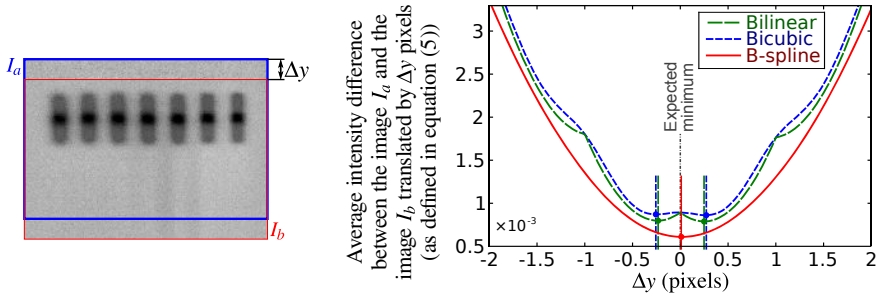

Figure 6: The classical bilinear and bicubic interpolation algorithms introduce a bias in the cost function of direct image registration. Unbiased results are obtained with our approach based on regularized B-splines. The curves on the right part of this figure have been obtained for a particular pair of images. Similar results are obtained for 420 other pairs of images.

approximately $\Delta y = \pm\frac{1}{3}$. Therefore, minimizing problem (4) using bilinear or bicubic interpolation would introduce a systematic bias.

To solve this problem, we convert the images to continuous functions during a preprocessing step. For that purpose we fit a regularized tensor product B-spline [17] to the intensities of the images. The control points $\mathbf{p}$ of the B-spline surface B approximating the image I are obtained by solving the following linear least-squares optimization problem [15]:

$$\min_{\mathbf{p}} \sum_{(x,y)\in\Omega} \left(B(x,y;\mathbf{p}) - I(x,y)\right)^2 + \lambda \iint_\Omega \left(\sum_{d=0}^{2} \frac{\partial^2 B}{\partial x^d \partial y^{2-d}}(x,y) \right)^2 \mathrm{d}x\mathrm{d}y, \tag{6}$$

where the first term measures the closeness of the surface to the image data and the second term penalizes the bending energy of the fitted surface. The parameter λ controls the trade-off between these two aspects. In practice, it is empirically set to a small value such as 10^{-6}. If we do the same experiment as the one described previously and replace the interpolation by a simple evaluation of the B-spline, the bias is drastically reduced (see figure 6).

4 Results

4.1 Data

The acquired video shows a pattern shaped as a horizontal row. The acquisition frequency was 50 Hz with an exposure time of $\frac{1}{300}$ second. Background subtraction and normalization techniques were applied to the raw data in order to correct the impurities of the Hele-Shaw cell and to compensate the temporal and spatial variations of the illumination source. Figure 7 shows examples of acquired images after correction.

Figure 8 sums up the main steps of the image correction process which may be described as:

1. Selection in the raw image of a region of interest containing the tagged pattern. On figure 8.1, we show the image corresponding to time $t = 1.32$ s in the video sequence presented in figure 7 ; that same image is reused for the other illustrations of figure 8.

2. Correction of the temporal variations of the source illumination during the video sequence. On figure 8.2, each blue dot represents the average grey level of one image. The red line represents the global variation across time (computed by fitting a polynomial of degree 3 to the blue dots). A global additive correction is applied to each image so that the resulting red line is flat (meaning that there is no global illumination variations in time).

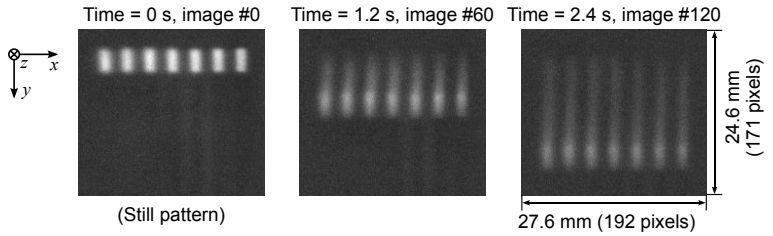

Figure 7: Images extracted from the input video at three different instants. These are images after correction (in particular, they are negative version of the original ones). Image #0 is acquired when the liquid is still and it is used as the reference image. Images #60 and #120 are acquired when the Poiseuille flow is fully developed.

3. Background extraction and subtraction. This step aims at removing, for each frame of the video, the flaws due to the impurities of our Hele-Shaw cell and the spatial variations of the illuminating laser. The background image is computed directly from the video sequence by keeping the brightest value across time for each pixel in the region of interest (figure 8.3 left). The background image is then subtracted to the frames of the video (figure 8.3 right).

4. Negative image. We work with negative images since it is more convenient to have low pixel values for the background and high pixel values for the tagged pattern (figure 8.4).

5. Removing the large spatial variations. While step 3 allowed us to remove the small spatial variations, this step allows us to remove the large scale ones. It is achieved by fitting a smooth two-dimensional surface to the data (figure 8.5 left) excluding the region of the image that contains the tagged pattern. The fitted surface (figure 8.5 center) is then subtracted to the data (figure 8.5 right).

6. The last step consists in cropping the image and adjusting the black level so that the pixel values for the background are zeros (figure 8.6).

4.2 Expected Results for the Poiseuille Flow

The underlying theory of the Poiseuille flow predicts that in steady state, the velocity profile across the cell is parabolic. Between the start of the draining off and the steady state, there exists a development phase during which the velocity profile smoothly evolves from a flat line (*i.e.* same velocity for all the points between the surfaces of the cell) to the parabola of the steady state (see, for instance, [18, 19]).

4.3 Illustration of our Generative Model

We visually inspect our model by comparing the acquired data to the initial pattern warped with the translations computed with our approach. Figure 9 shows an example where the two images match which means that our approach is valid. Similar results were obtained for the other images of the video.

4.4 Computed Translations and Velocity Profiles

Figure 10 shows the velocity profiles in the direction of the z-axis (*i.e.* the cell's gap) at four different instants. The thickness of the cell was discretized into 40 layers. The velocity profiles are computed from the whole row of marks. The profile computed for image #8 corresponds to a time where the flow is in a transitory state. Figure 10 also shows that the profiles computed for images #44, #80, and #115 are well fitted by a parabola which confirm the fact that the computed flow is consistent with the theoretical Poiseuille flow model for the steady state. A quantitative measure reinforces this fact: for instance, on image #115, the maximal velocity (reached at the center of the cell) is of 6.48 mm.s^{-1} (0.9 pixel.image^{-1}). The next experiment reveals that

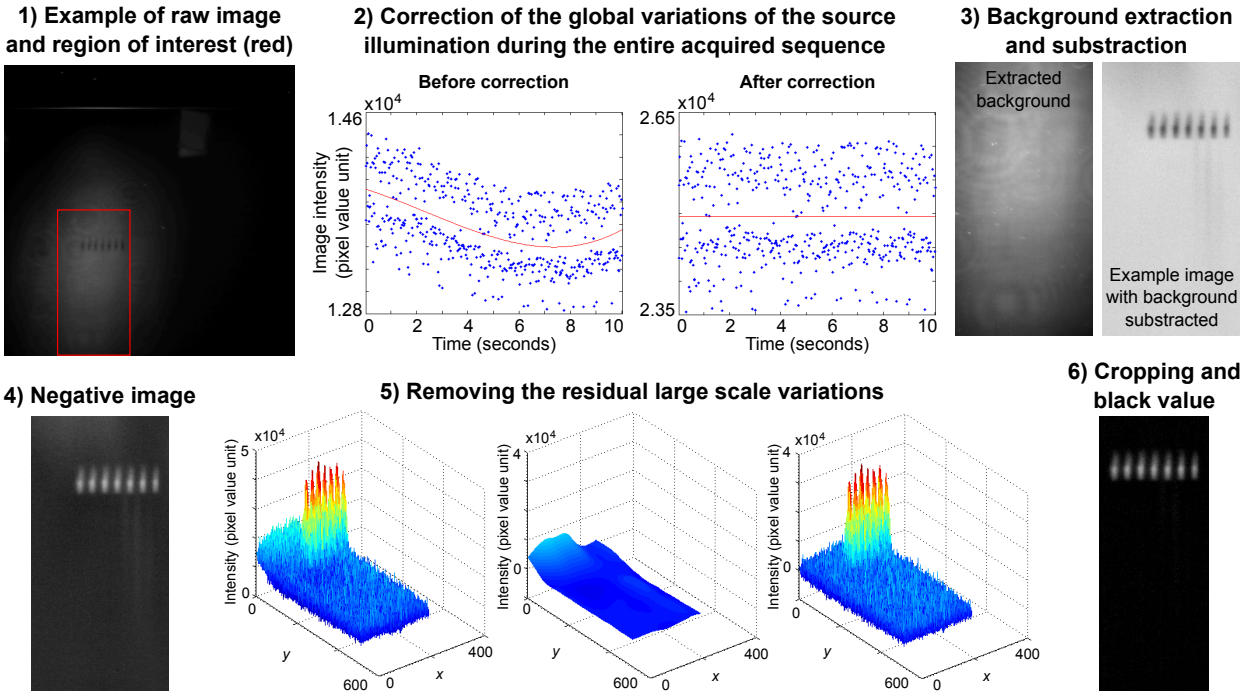

Figure 8: The different steps of the image correction process. Explanations and details are in the text (see 4.1).

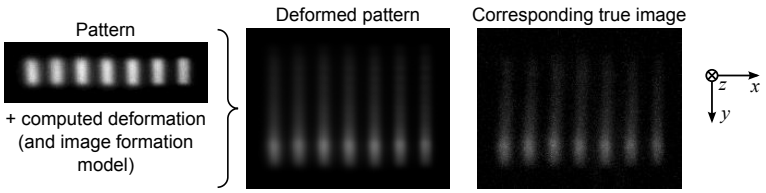

Figure 9: Comparison between the initial pattern warped using the translations computed with our approach and the corresponding true image of the video.

the actual average velocity is 4.17 mm.s^{-1} (0.58 pixel.image^{-1}). The ratio between these two values is 1.55 which is very close to 1.5, the theoretical value expected for a Poiseuille flow.

The water/air interface being visible in the field of view of the camera (see figure 11a), it is possible to quantitatively evaluate the accuracy of the velocities computed with our approach. For that purpose, we compare the velocities of the molecular tagging (averaged along the x and the z axes) with the ones of the free surface of the liquid. The results are reported in figure 11b. By averaging over time the velocity measured with our approach when the Poiseuille flow is established, we obtained a velocity of 4.38 mm.s^{-1} (0.61 pixel.image^{-1}) whereas the one computed from the motion of the water/air interface is of 4.17 mm.s^{-1} (0.58 pixel.image^{-1}). The discrepancy between these two experimental measurements is therefore about 0.2 mm.s^{-1} (0.03 pixel.image^{-1}) which is very small and which is less than the inaccuracies typically encountered for other techniques of velocimetry [20].

Figure 12 shows a 3D representation of the volume reconstructed with our approach. The parabolic displacement of the layers is seen on the side of the illustrations. The position of this parabolic displacement is consistent with what is actually observed by the camera.

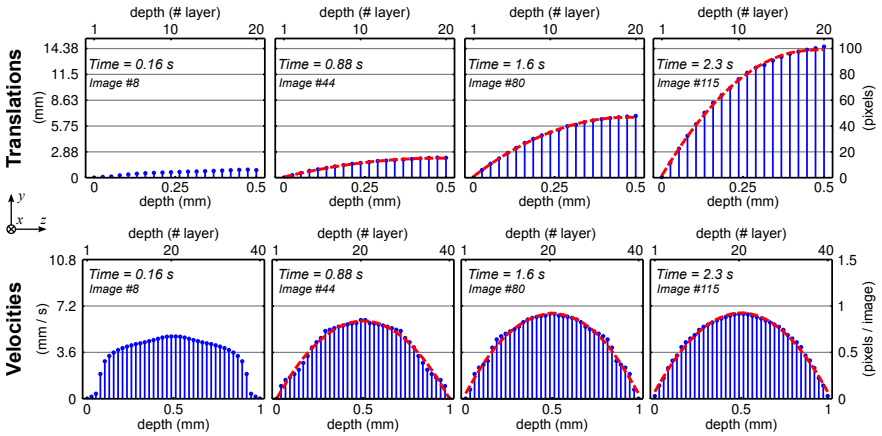

Figure 10: Computed translations (top) at different times and corresponding velocities (bottom). Image #8 is taken when the Poiseuille flow is developing whereas images #44, #80, and #115 correspond to an established Poiseuille flow. When the steady flow is established, a polynomial of degree 2 is fitted to the computed data (dashed red curves): it shows that our results and the theoretical flow are consistent (more details in the text).

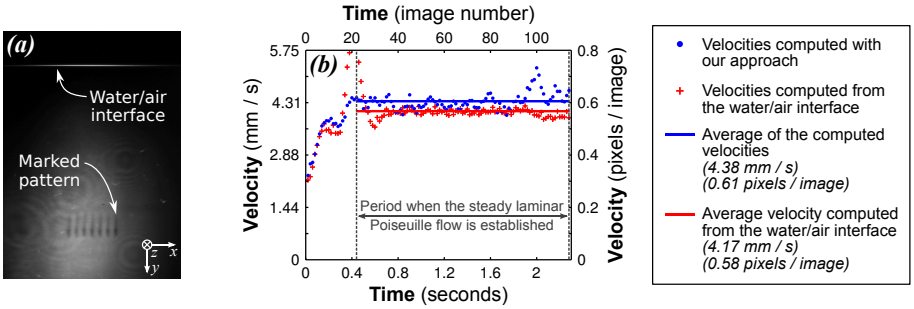

Figure 11: (a) The water/air interface is visible in the raw images. (b) Comparison of the velocities computed with our approach (averaged over the cell gap) and the average velocity computed from the water/air interface.

5 Discussion and perspectives

We have proposed a new algorithm that can track the motion of a liquid in a Hele-Shaw cell being drained while simultaneously computing a full volumetric reconstruction of the inner part of the cell from a single point of view. The photobleaching MTV technique has been extended to 3D measurements and is well suited for flows in confined environment with limited optical access. We built our approach on top of direct image registration to which we added supplementary hypotheses to properly constrain the reconstruction problem. However, we have taken special care to use general enough assumptions on the physical flow model so as to make significant physical measurements. This allowed us to experimentally measure the establishment of the Poiseuille flow in a confined environment and for a large volume.

In this paper, we have shown that our method is able to measure unsteady flows inhomogeneous in the direction perpendicular to the gap of the cell. A possible next step of our work will be to handle flows with inhomogeneity in the plane of the cell. A possible extension of this future work would be to study the flow around air bubbles rising in the cell.

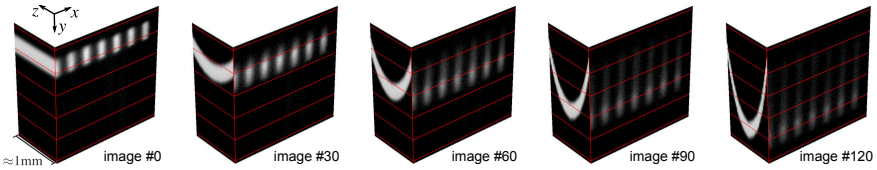

Figure 12: 3D representation of the reconstructed volume. The parabolic Poiseuille flow is visible on the edge and its position is consistent with what is seen at the cell front.

Acknowledgement The authors gratefully acknowledge the financial support of Fédération de recherche Fermat. We also thank Sébastien Cazin for his help on the technical aspects of image acquisition.

References

[1] H. Stone, A. Stroock, A. Adjari, Engineering flows in small devices: Microfluidics toward a lab-on-a-chip, Annu. Rev. Fluid Mech. 36 (2004) 381–411.

[2] D. Sinton, Microscale flow visualization, Microfluidics and Nanofluidics 1 (2004) 2–21.

[3] M. Roudet, A. M. Billet, V. Roig, F. Risso, S. Cazin, E. Cid, PIV method with volumetric lighting for measurements in narrow channel: Application to the flow around a rising bubble, in: International Symposium on Flow Visualization, 2008, pp. 1–8.

[4] R. Szeliski, Image alignment and stitching: A tutorial, Foundations and Trends in Computer Graphics and Vision 2 (2006) 1–104.

[5] I. Ihrke, K. Kutulakos, H. Lensch, M. Magnor, W. Heidrich, State of the art in transparent and specular object reconstruction, in: STAR Proceedings of Eurographics, 2008, pp. 87–108.

[6] G. T. Herman, Fundamentals of Computerized Tomography: Image Reconstruction from Projections, 2nd Edition, Springer, 2009.

[7] M. Magnor, G. Kindlmann, C. Hansen, N. Duric, Constrained inverse volume rendering for planetary nebulae, in: IEEE Visualization (Vis'04), 2004, pp. 83–90.

[8] T. Hawkins, P. Einarsson, P. Debevec, Acquisition of time-varying participating media, in: SIGGRAPH, 2005, pp. 812–815.

[9] C. Garbe, K. Roetmann, V. Beushausen, B. Jahne, An optical flow MTV based technique for measuring microfluidic flow in the presence of diffusion and Taylor dispersion, Experiments in Fluids 44 (2008) 439–450.

[10] M. Roudet, A. Billet, F. Risso, V. Roig, PIV with volume lighting in a narrow cell: An efficient method to measure large velocity fields of rapidly varying flows, Experimental Thermal and Fluid Science 35 (2011) 1030–1037.

[11] S. Hosokawa, A. Tomiyama, Molecular tagging velocimetry based on photobleaching reaction and its application to flows around single fluid particles, Multiphase Science and Technology 16 (2004) 335–353.

[12] S. Hosokawa, T. Fukunaga, A. Tomiyama, Application of photobleaching molecular tagging velocimetry to turbulent bubbly flow in a square duct, Experiments in Fluids 47 (2009) 745–754.

[13] C. Besnaci, Mélange induit par un écoulement à travers un réseau aléatoire de sphères, Ph.D. thesis, Institut National Polytechnique de Toulouse, France (2012).

[14] R. Hartley, A. Zisserman, Multiple View Geometry in Computer Vision, 2nd Edition, Cambridge University Press, 2004.

[15] Å. Björck, Numerical Methods for Least Squares Problems, Society for Industrial and Applied Mathematics, 1996.

[16] R. Fletcher, Practical Methods of Optimization, John Wiley and Sons, 1987.

[17] P. Dierckx, Curve and Surface Fitting with Splines, Monographs on Numerical Analysis, Oxford University Press, 1993.

[18] T. Caplow, www.columbia.edu/cu/gsapp/bt/research/arch-atmos/u_double.gif.

[19] A. Hifdi, J. K. Naciri, Étude analytique de perturbations de l'écoulement de Poiseuille dans un canal, Comptes Rendus Mecanique 332 (3) (2004) 241 – 248.

[20] M. Stanislas, K. Okamoto, C. Kähler, J. Westerweel, F. Scarano, Main results of the third international PIV challenge, Experiments in Fluids 45 (2008) 27–71.

[21] A. Efros, V. Isler, J. Shi, M. Visontai, Seeing through water, in: Neural Information Processing Systems (NIPS 17), 2004.